Doped Bilayer Tin(IV) Oxide Electron Transport Layer for High Open-Circuit Voltage Planar Perovskite Solar Cells with Reduced Hysteresis

Jiajiu Ye, Yuze Li, Asma Aicha Medjahed, Stéphanie Pouget, Dmitry Aldakov, Yueli Liu, Peter Reiss

Doped Bilayer Tin (IV) Oxide Electron Transport Layer for High Open Circuit Voltage Planar Perovskite Solar Cells with Reduced Hysteresis

Jiajiu YE,[1,*] Yuze LI,[1] Asma MEDJAHED,[1] Stéphanie POUGET,[2] Dmitry ALDAKOV,[1] Yueli LIU,[3,*] Peter REISS[1,*]

[1]*Univ. Grenoble-Alpes, CEA, IRIG/SyMMES, STEP, 38000 Grenoble, France*

[2]*Univ. Grenoble-Alpes, CEA, IRIG/MEM, SGX, 38000 Grenoble, France*

[3]*State Key Laboratory of Silicate Materials for Architectures, School of Materials Science and Engineering, Wuhan University of Technology, Wuhan, 430070, P. R. China*

Abstract: SnO_2 is an emerging electron transport layer (ETL) material in halide perovskite solar cells, outperforming more widely used TiO_2 in several aspects, such as conductivity and transparency. Among current limitations, open-circuit voltage (V_{OC}) loss is one of the major factors to be addressed for further improvement. Here we propose a bilayer ETL consisting of two SnO_2 nanoparticles layers doped with different amounts of ammonium chloride. As demonstrated by combined XPS/UPS and photophysical studies, the main effect of the novel ETL is to modify the energy level alignment at the SnO_2/perovskite interface, which leads to decreased carrier recombination, enhanced electron transfer and reduced voltage loss. Moreover, X-ray diffraction reveals reduced strain in perovskite layers grown on bilayer ETLs with respect to single layer ETLs, further contributing to a decrease of carrier recombination processes. Finally, the bilayer approach enables the more reproducible preparation of smooth and pinhole-free ETLs as compared to single-step deposition ETLs. Perovskite solar cells with the doped bilayer SnO_2 ETL demonstrate strongly increased V_{OC} values of up to 1.21 V with a power conversion efficiencies of 21.75% while showing negligible hysteresis and enhanced stability. Moreover, the SnO_2 bilayer can be processed at low temperature (70°C), and has therefore a high potential for use in tandem devices or flexible perovskite solar cells.

Introduction

Due to excellent photovoltaic performance of perovskite solar cells (PSCs) and low fabrication costs, they are considered as one of the most promising emerging photovoltaic technologies. In only one decade, the power conversion efficiency (PCE) of single-junction

PSCs has increased up to 25.2%.[1-4] Currently, the planar structure is one of the main architectures of perovskite solar cells, as it can be prepared by a simple and reproducible fabrication process. The n-i-p architecture of such planar PSCs consists of a transparent cathode (ITO or FTO), an electron transport layer (ETL), the perovskite light harvesting layer, a hole transport layer (HTL), and an anode (e.g., Au or Ag). Electron transport and hole blocking capacity, high charge carrier extraction rate and low recombination rate are critical parameters for the ETL. Titanium oxide (TiO_2) and zinc oxide (ZnO) have been most widely used as n-type ETL materials in PSCs. However, a number of shortcomings such as low conductivity, low electron mobility, surface metal interstitials, oxygen vacancies and UV instability, were shown to produce defects and trap states, which could cause undesired recombination of photo-generated carriers.[5-9] More recently, tin oxide (SnO_2) has been shown to be a highly promising alternative ETL material. Compared to TiO_2 and ZnO, SnO_2 has a higher conductivity, better optical transmittance and wider band gap. Contrary to the most widely used ETL material TiO_2, SnO_2 also provides the possibility of low-temperature processing. The reported electron mobility of SnO_2 is up to 1.2×10^{-3} cm^2 $V^{-1}s^{-1}$, i.e. two orders of magnitude higher than that of TiO_2.[10] Furthermore, the larger bandgap of SnO_2 (above 3.6 eV *vs.* 3.2 eV) contributes to a smaller short circuit current loss. Finally, PSCs using SnO_2 ETLs have been shown to be more stable than TiO_2 based devices under UV illumination, due to the lower photocatalytic activity.[11-13] All these factors contribute to the high potential of SnO_2 for use as ETL in various types of PSCs, encompassing flexible or Si/perovskite tandem solar cells.

In 2015, Ma *et al.* reported nanocrystalline SnO_2 as ETL in PSCs using the sol-gel technique. However, the devices demonstrated a comparably low open-circuit voltage (V_{OC}) and fill factor (FF) due to charge recombination processes caused by oxygen vacancies.[14] Meanwhile, to increase the photovoltaic performances, intense studies have been devoted to the modification of the SnO_2 ETL, such as interface passivation, doping, and surface treatments.[15-16] Zhang *et al.* developed a low temperature processed SnO_2 thin film modified by fullerene ($PC_{60}BM$) as effective ETL. The introduction of $PC_{60}BM$ resulted in a lower trap state density and higher electron mobility. In addition, the crystalline quality and grain boundary integration in perovskite films could be enhanced, which led to strongly increased performance of the planar PSCs.[18] Li *et al.* fabricated a hybrid ETL of SnO_2 and carbon nanotubes (CNTs) by a simple

thermal decomposition method. The addition of CNTs significantly improved the conductivity of the SnO_2 films and reduced the trap-state density, resulting in an efficiency of 20.33%, strongly enhanced compared to the conventional device without CNTs (PCE=17.90%).[19] More recently, both the teams of L. Li and G. Fang reported PSCs using ammonium chloride doped SnO_2 nanoparticles as ETL. Enhanced electron extraction and transport, and a more suitable energy band alignment were the main factors identified to contribute to the observed improvement of PCE and V_{OC}, yielding values of 19.93% and 21.38% (PCE) as well as 1.19 V and 1.15 V (V_{OC}), respectively. [20, 21]

Despite these advances, it remains very challenging to achieve single-layer electron transport materials without pinholes and hence optimal ability to block holes. Any pinholes in the ETL will lead to the direct contact between the transparent conducting oxide substrate and the perovskite layer, resulting in charge carrier recombination, voltage losses and current leakage.[22-24] In this context, the use of bilayer ETLs has been shown to be a very appealing strategy. In the general case, bilayer ETLs can be constituted of different materials, however, the abrupt interfaces in the resulting heterojunction bilayers can give rise to undesirable voltage losses and carrier recombination processes. A typical example is the TiO_2/SnO_2 bilayer ETL with reported device performances of 20.3% (PCE) and 1.13 V (V_{OC}) in 2019[25] and earlier 15.39%/0.98 V.[26] The use of a homojunction bilayer ETL appears as an interesting alternative from many points of view, e.g., smooth energetic interface, chemical compatibility, strain-free growth. Uddin and coworkers reported the use of a non-doped homojunction ETL by depositing SnO_2 nanoparticles onto a sol-gel SnO_2 layer with the goal to fill the pin-holes of the latter (PCE: 17.61%, V_{OC}: 1.07 V). [27]

In this work, we explore a different way to create an efficient homojunction bilayer ETL by combining two SnO_2 nanoparticle layers of different doping levels with ammonium chloride. It is expected that ammonium salt doped bilayers increase the charge transfer rate and, at the same time, induce a favorable band alignment well matched with the perovskite. Therefore, for an optimized architecture both charge separation at the SnO_2/perovskite interface and transport in the ETL should be effectively accelerated, resulting in reduced charge accumulation.[28-30] Several types of SnO_2 ETLs were fabricated, pristine, low-amount-doped SnO_2 and high-amount-doped SnO_2 being abbreviated as P-SnO_2, L-SnO_2 and H-SnO_2, respectively. The best-

performing doped bilayer, denoted as B-SnO_2, was obtained by depositing a H-SnO_2 layer on top of a L-SnO_2 layer and annealing at a temperature as low as 70°C. A comprehensive study of devices containing the different types and combinations of SnO_2 ETLs demonstrates that B-SnO_2 based solar cells exhibit an enhanced average FF and V_{OC} compared with those of P-/L-/H-SnO_2 single-layer ETLs and reverse B-SnO_2 ETLs (L-SnO_2 on top of H-SnO_2). Combined XPS/UPS, photophysical and structural studies reveal that these improvements stem from enhanced charge transport and reduced photogenerated carrier losses. The best performing PSC device yielded a PCE of 21.75% and showed negligible hysteresis with a maximum V_{OC} of 1.21 V, presenting an almost 20% enhancement compared to P-SnO_2. Moreover, the bilayer ETL device showed a 15% lower degradation rate compared to single layer devices, indicating superior stability due to less defects and the absence of charge accumulation at the ETL/perovskite interface.

Results and discussion

SnO_2 ETLs with different doping levels of ammonium chloride (undoped/pristine: P-SnO_2; low amount (20 mmol/mL): L-SnO_2; high amount (40 mmol/mL): H-SnO_2; bilayer L+H: B-SnO_2) were prepared by spin-coating aqueous solutions containing SnO_2 nanoparticles and NH_4Cl on ITO-coated glass substrates, followed by annealing for 1 h at 70 °C in air (cf. Supporting Information: Experimental Part and **Figure S1**). The used commercial SnO_2 nanoparticles had a mean size of around 4-6 nm and their colloidal character enabled a smooth and continuous coating of SnO_2 thin layers on the ITO substrates.

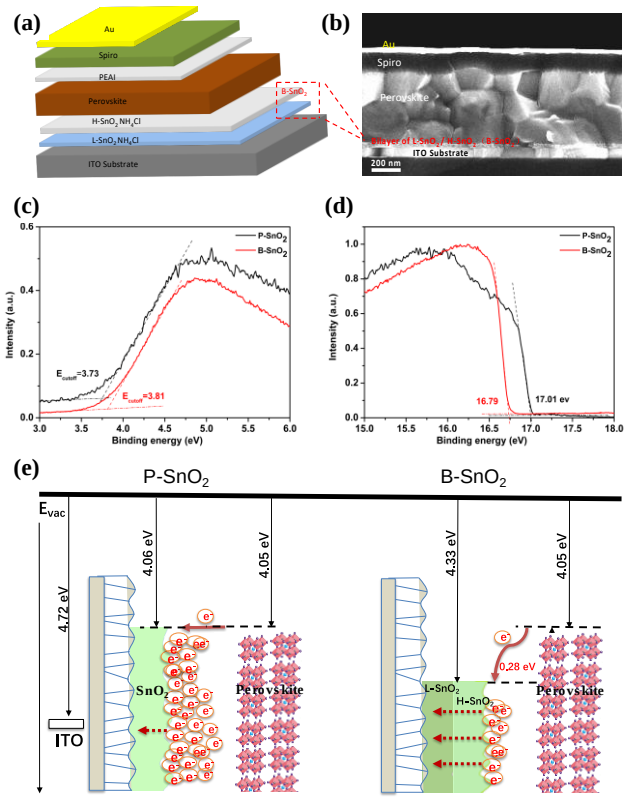

Figure 1. (a) Schematic view of the device structure. (b) Corresponding cross-sectional SEM image of the device. (c, d) UPS spectra on pristine single layer (P-SnO_2) and NH_4Cl-doped bilayer (B-SnO_2) SnO_2 thin films deposited on ITO; c) Fermi level determination; d) secondary edge region. (e) Schematic diagram of the electron extraction process for both types of ETL and energy level diagram.

A scheme of the solar cell device architecture is shown in **Fig. 1a** and an SEM cross-sectional view in **Fig. 1b**. The PSC has a regular n-i-p architecture with a doped bilayer ETL, which has the purpose of enhancing charge carrier extraction from the perovskite layer. The L-SnO_2 and H-SnO_2 layers have differences in carrier concentration but share common material properties. Therefore, their combination has less interfacial resistance as well as decreased energy loss during electron transfer in the two ETL layers. Ultraviolet photoelectron spectroscopy (UPS) measurements and UV-vis absorption spectroscopy were carried out to investigate the energy level structure of the two types of ETLs (cf. **Fig. S2a**). The work function of pristine P-SnO_2 and of the doped bilayer B-SnO_2 are estimated to be -4.21eV and -4.43eV, respectively, by subtracting the binding energy of the secondary edge of the samples (17.01 eV and 16.79 eV) from the excitation energy of the UV photons (21.22 eV, He I UPS) spectra (**Fig. 1d**). From the

UPS cutoff levels, the energy difference between the valence band maximum (VBM) and the Fermi level (Φ) are estimated to be 3.73 eV and 3.81 eV for SnO_2 and B-SnO_2, resulting in E_{VB} = -7.94 eV and -8.24 eV, respectively (cf. **Fig. 1c** and **S3**). **Figure S2b** depicts the Tauc plots of each type of ETL film, from which the optical bandgaps can be deduced. The band gap of B-SnO_2 (3.91 eV) is slightly higher than that of H-SnO_2, L-SnO_2 and pristine SnO_2 (3.905, 3.90 and 3.89 eV), albeit all values are very close. Using these values, the conduction band minimum (CBM) levels were calculated as -4.06 eV and -4.33 eV for P-SnO_2 and B-SnO_2, respectively (**Fig. S3**). Taking the CBM value of the triple cation (CsFAMA) perovskite, determined by Abate and coworkers via UPS as -4.05 eV,[31] reveals a flat energy level alignment in the case of P-SnO_2, while for B-SnO_2 an energy offset of 0.28 eV exists (**Fig. 1d**). Therefore, more efficient electron extraction can be expected in the latter case due to the energetic driving force at the ETL/perovskite interface.

The charge transport properties within the ETL are a further important parameter for effectively extracting photo-induced electrons and transferring them to the anode. Typically, the electron mobility in the perovskite layer is on the order of 10^3-10^2 cm^2/Vs, [32] i.e. much higher than in SnO_2 ETLs (approximately 10^{-3} cm^2/ Vs), [33] causing electron accumulation at the ETL surface. Cl-doping has been shown to significantly increase the electron mobility in single-layer SnO_2 ETLs, up to a factor 3.5.[20] Due to the higher electron mobility (μ_e) in the ETL, charges can be evacuated more quickly at the perovskite/ETL interface, as illustrated in **Fig. 1d**. By consequence, devices with the L-SnO_2/H-SnO_2 bilayer ETL exhibit a higher V_{OC} (*vide infra*) taking advantage of both the aforementioned larger free energy offset (ΔG) between E_{CB} of the perovskite and E_{CB} of the ETL as well as the higher electron mobility of the doped SnO_2 ETL. These factors lead to enhanced electron injection from the perovskite into the ETL and reduced charge accumulation at ETL surface. In addition, the deeper lying Fermi level of the bilayer ETL (-4.43 eV *vs*. -4.21 eV) also contributes to the electron extraction ability from the perovskite layer and increased device performance.

To study the surface topology of the obtained ETLs, electron microscopy has been used. Scanning electron microscopy (SEM) indicates homogeneous surface coverage with SnO_2 nanoparticles (**Fig. S4**), however, this technique does not allow for a more precise analysis of the surface roughness. Therefore, atomic force microscopy (AFM) was performed (**Fig. 2a**).

All four SnO_2 films (pristine, L-SnO_2, H-SnO_2 and B-SnO_2) showed a similar morphology, albeit the surface roughness increased slightly from 2.49 nm to 2.84 nm (RMS) when comparing P-SnO_2 and B-SnO_2. Comparing the doped ETLs, the surface roughness of B-SnO_2 (2.84 nm) was lower than that of the single-layer ETLs (2.99 nm for L-SnO_2, 3.17 nm for H-SnO_2). This can be attributed to the filling of pin-holes and defects on the surface of L-SnO_2 during the second spinning cycle. The obtained better surface coverage results in the reduction of recombination sites, preventing from detrimental carrier losses.

Fig. 2b depicts the transmittance spectra of each type of ETLs films. P-SnO_2/ITO exhibited the highest transmittance in the visible region (89.4%), followed by L-SnO_2/ITO (88.7%), H-SnO_2/ITO (88.3%) and B-SnO_2/ITO (87.8%). However, these values are very close, proving that the use of a double layer did not strongly decrease the optical performance of the film, i.e., the transmittance of the novel ETL was still high enough to ensure the efficient absorption of sunlight in the perovskite layer. Similar to the transmittance spectra, the UV absorption spectra of the different ETL layers on ITO-coated glass showed only very small differences (**Fig. S5**).

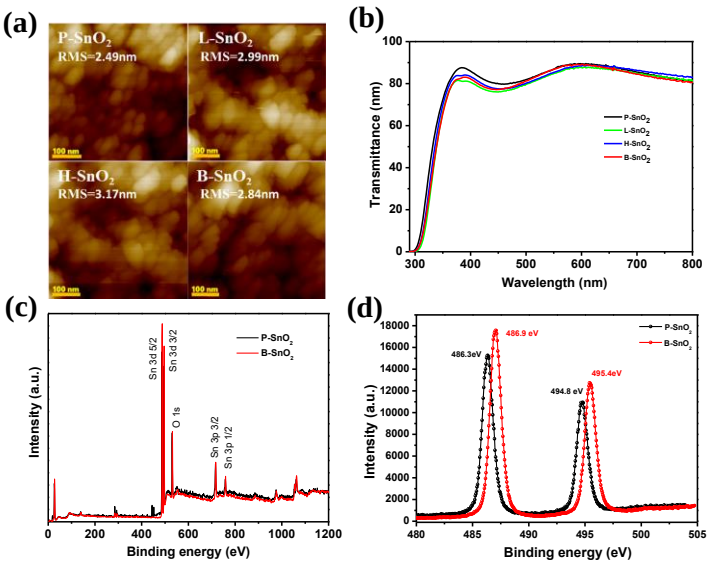

Figure 2. (a) AFM images of the different types of SnO_2 ETLs deposited on ITO substrates and surface roughness (root mean square average). (b) Transmittance spectrum of SnO_2 thin films on ITO glass. (c) XPS survey spectrum and (d) enlarged view of the Sn 3*d* region of the P-SnO_2 and B-SnO_2 films.

XPS measurements were carried out to study the surface states of the ETL thin films. A weak signal of carbon C1s (284.6 eV) indicated a very low amount of organic residues on the surface

and thus extremely low surface contamination. The spectra at the Sn edge with the attribution of the corresponding peaks are depicted in **Figure 2c**. The peaks located at 486.9 eV and 495.4 eV (**Fig. 2d**) are corresponding to Sn 3d5/2 and Sn 3d3/2 states, confirming that SnO_2 was the primary chemical component. These peaks were shifted to higher binding energy by around 0.6 eV in the case of B- SnO_2 when comparing with P-SnO_2, demonstrating a decrease of electron density at the Sn atoms, which is equivalent to their stronger oxidation and filling of oxygen vacancies. Photoluminescence (PL) spectra were recorded to further study the trap states in P-/B-SnO_2 ETLs. The SnO_2 thin films exhibited a broad emission peak centered around 390 nm and extending beyond 500 nm, as shown in **Fig. S6**. Oxygen vacancies are the main luminescence centers in SnO_2 for emission in the visible range and give rise to the observed trap emission.[34] As compared to P-SnO_2, the emission in the range of 420-500 nm decreased in B-SnO_2, indicating once again a reduced density of oxygen vacancies, which contributes to the enhancement of FF in the PSC device (*vide infra*).

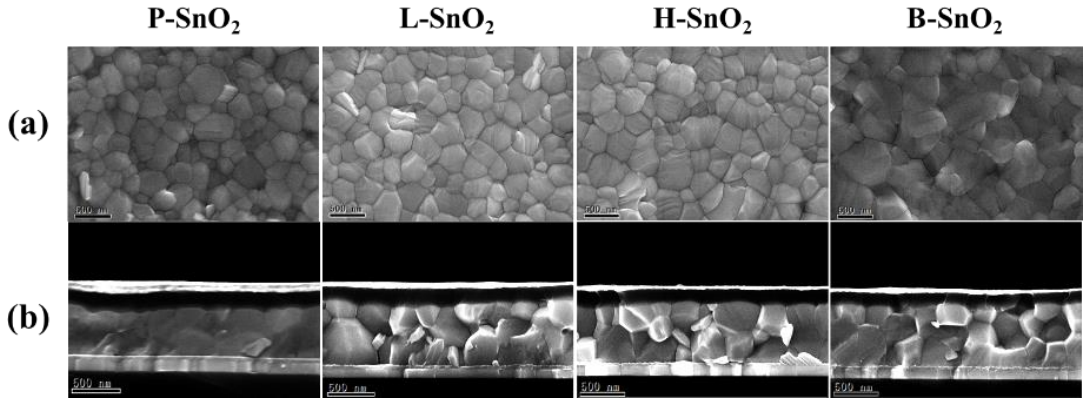

Figure 3. (a, b) Top-view and cross-section view scanning electron microscopy (SEM) images of perovskite films deposited on P-/L-/H-/B-SnO_2 ETLs. The scale bar is 500 nm.

In the next step, PSC devices in the planar configuration ITO/ETL/perovskite/Spiro/Au were fabricated using these ETLs. To study the influence of the different SnO_2 ETLs on the perovskite film properties, first surface and cross-sectional morphologies were characterized using SEM (**Fig. 3a**). From the top-view images, average perovskite crystallite sizes of 100-400 nm are visible on the P-SnO_2 film, while in the case of B-SnO_2 larger sizes of approximately

800 nm can be observed. This is a clear evidence that the underlying ETL affects the morphology of the perovskite layer. The dense packing of larger grains in B-SnO_2 as visible in Figure 3b reduces the number of trap states generated at grain boundaries. To the contrary, perovskite films on P-SnO_2 showed crystallite sizes around 200 nm and exhibited more cross-sectional crystal boundary defects, indicating poor crystallization. In the series of L-/H-/B-SnO_2 substrates, the perovskite grain size increased gradually. Therefore, it can be concluded that doping of SnO_2 with ammonium chloride has a significant impact on perovskite nucleation and growth. In the case of B-SnO_2, the growth of large and densely packed perovskite grains improves the charge carrier collection efficiency as it results in reduced charge trapping and recombination within the perovskite layer.[35] The surface roughness of the perovskite films was investigated using AFM, as illustrated in **Table S1**. Perovskite films on P-SnO_2 have the smallest crystal size and highest surface roughness of 26.2 nm RMS. For perovskite films deposited on L-SnO_2, H-SnO_2 and B-SnO_2, the corresponding surface roughness decreased from 20.2 nm to 18.4 nm and finally 17.3 nm, becoming gradually smoother. Concluding, SEM and AFM analyses show that the bilayer SnO_2 ETL not only results in the largest crystallite sizes after perovskite deposition, but also maintains a low surface roughness, even slightly smoother than with the other ETLs.

Figure 4(a) shows the XRD patterns of the triple cation perovskite films grown on P-SnO_2 and B-SnO_2 ETLs, with the main diffraction peaks located at 14.06°, 28.47° and 31.94°. They can be assigned to the (001), (002) and (012) reflections, respectively, of the CsFAMA cubic crystalline phase (space group m-3m).[36] The other peaks at 19.97°, 24.55°, 40.87° and 43.52° are associated with the (011), (111), (022) and (003) reticular planes. We can also observe a strong diffraction peak at 12.68° indicating the presence of excess PbI_2, which can passivate grain boundaries.[37] A slight shift of the diffraction peaks to larger angles is observed in the case of B-SnO_2 (**Fig. 4b**) and the lattice parameters of the cubic triple cation perovskite on P-SnO_2 and on B-SnO_2 are 6.278(2)Å and 6.272(2)Å, respectively.

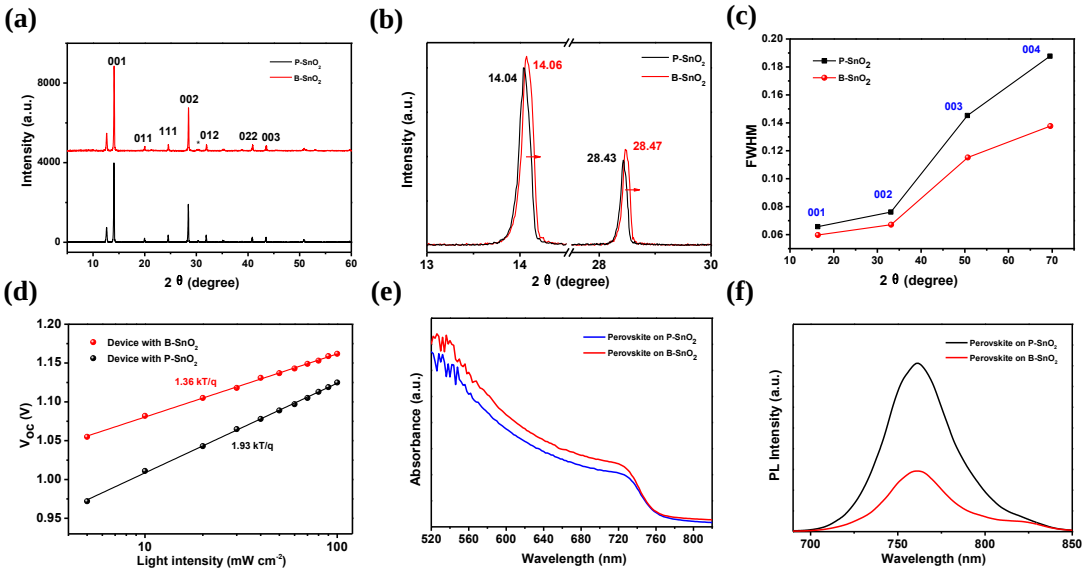

Figure 4. (a,b) XRD patterns of CsFAMA perovskite films deposited on top of P-/B-SnO_2 ETLs. (c) Peak widths (FWHM) of the different (00l) perovskite diffraction peaks. (d) V_{OC} dependency on the light intensity of devices based on P-/B-SnO_2 substrates. (e) UV–vis spectra of the perovskite films. (f) Steady-state photoluminescence spectra of perovskite films prepared on each type of ETL (the shoulder at around 820 nm is an artefact of the detector).

The observed smaller lattice constant of the film may be partially attributed to the higher ratio of the bilayer dopants NH_4^+ and Cl^- in the FA-based perovskite lattices. **Figure 4c** displays the evolution of the full width at half maximum (FWHM) of the (00l) diffraction peaks of the two samples. Considering the instrumental resolution, these values indicate that the perpendicular crystallite size is larger than 100 nm, which is coherent with the SEM observations. The observed increase of the FWHM values for the higher diffraction orders traduces the presence of distorsion (strain) in the lattice. This distorsion appears to be maximum for the P-SnO_2 perovskite film. We further studied whether carrier recombination processes of the devices were affected by the strain. **Fig. 4d** shows the relationship between V_{OC} and light intensity. If the slope of V_{OC} versus light intensity is larger than kT/q, additional recombination caused by strain is involved,[2] where q is the electron charge, k is the Boltzmann constant, and T is the Kelvin temperature. It can be seen that the P-SnO_2 devices showed a slope of 1.93kT/q, while ammonium doped B-SnO_2 devices showed a smaller slope (1.36kT/q). There is no

obvious charge barrier induced at the interface when B-SnO_2 was introduced. These results further confirm that carrier recombination has largely been suppressed in the perovskite layer.

UV-vis absorption spectroscopy was used to measure the absorbance of the perovskite films on each type of the SnO_2 substrates (**Fig. 4e**). The films showed similar absorption spectra, although the film on the bilayer exhibited slightly enhanced absorbance and hence light harvesting despite of its identical thickness compared with the other films (cf. **Fig. 3**), which could lead to a higher J_{SC} of the PSC device. Steady-state photoluminescence (PL) spectroscopy (**Fig. 4f**) reveals an emissive band of the perovskite peaking around 762 nm for all types of ETL. The PL intensity is strongly reduced in the case of the B-SnO_2 ETL, which showed a significant quenching effect. This behavior suggests that the perovskite film on the bilayer ETL exhibits faster charge transfer kinetics, which can effectively decrease charge carrier recombination in the active layer of the PSC, contributing to a higher J_{SC} and FF in the devices.

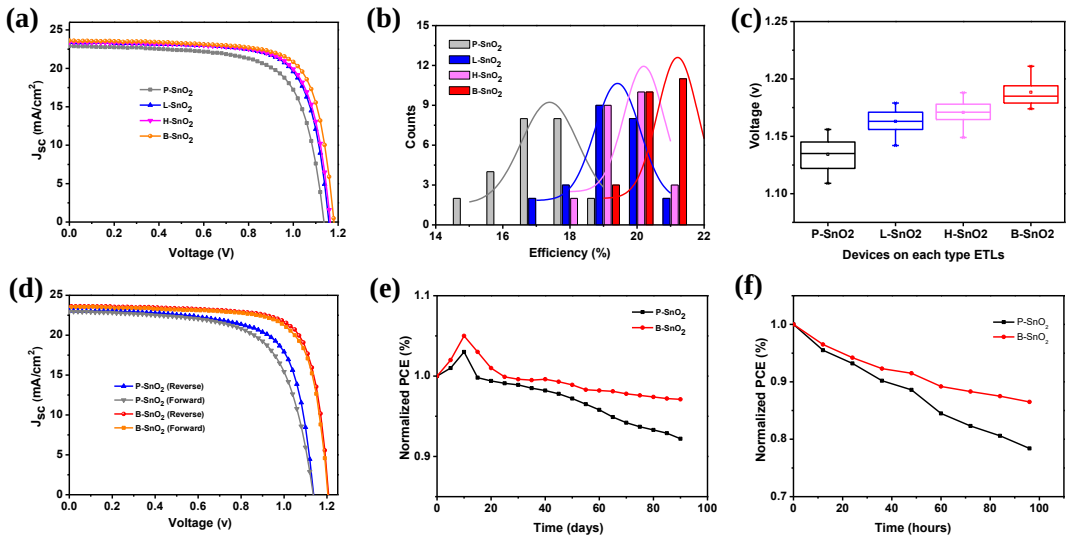

Figure 5. (a) Photovoltaic characteristics of PSCs using P-SnO_2, L-SnO_2, H-SnO_2, and B-SnO_2 ETLs. (b) Efficiency distribution of perovskite solar cells. (c) Comparison of the device V_{OC} distribution on each ETL. (d) J-V curves of reverse and forward scans for B-SnO_2 and pristine SnO_2 devices. (e) Long-term stability measurements of devices based on P-SnO_2 and B-SnO_2 ETL without encapsulation under N_2 atmosphere. (f) Stability test of perovskite devices under continuous light illumination (AM1.5) at room temperature, and measured after each 12 h.

Based on the above analysis, we expect that the bilayer ETL would be beneficial for both boosting the device performance and lowering hysteresis in planar PSCs, due to the more favorable energy level alignment and absence of charge accumulation at the perovskite/ETL interface. Optimization of the thicknesses of the different layers showed that ETLs of 40 nm exhibited the highest photovoltaic performances and for the perovskite film, spiro-OMeTAD, and the Au electrode the best values were found to be around 700, 200, and 80 nm, respectively. The corresponding J/V curves of devices obtained by low temperature processing is shown in **Figure 5a**. The pristine SnO_2 device demonstrated a lower PCE of 18.19% with marked hysteresis. We attribute this behavior to the presence of pinholes in the ETL and recombination losses at the ETL/perovskite interface. Devices based on L-SnO_2 and H-SnO_2 showed a significant improvement, and achieved higher efficiencies of 19.92% and 20.13%, respectively. The performances of devices prepared with B-SnO_2 was further increased to 20.83%. These PCE results agree well with the properties of the ETL/perovskite layers discussed above. The advantages of less pinholes, higher perovskite crystallinity, larger grain size, and higher absorbance brought by the B-SnO_2 ETL, led to devices with less recombination losses. Compared to PSCs based on single-layer SnO_2, devices integrating the bilayer SnO_2 resulted in better performances. The detailed J-V parameters are illustrated in **Table S4**, and the statistical distribution of the efficiencies of the devices tested are shown in **Figure 5b**. The average V_{OC} value of P-SnO_2 devices was 1.134 V, but higher values of 1.163 V (L-SnO_2), 1.171 V (H-SnO_2), and 1.189 V (B-SnO_2) were obtained with the other ETLs, demonstrating unambiguously a V_{OC} enhancement (**Fig. 5c**). **Figure 5d** shows the reverse and forward scan *J-V* curves of the champion cells for devices based on bilayer and pristine SnO_2. The P-SnO_2 based PSCs achieved a best PCE of 18.54 % with J_{SC} of 23.0 mA/cm^2, V_{OC} of 1.137 V and FF of 0.698, while the champion PCE of B-SnO_2 based PSCs was 21.75% along with J_{SC} of 23.6 mA/cm^2, V_{OC} of 1.208 V and FF of 0.762. The devices also showed lower *J-V* hysteresis with a hysteresis index of 6.9% and 2.4% for the P-SnO_2 and B-SnO_2 based devices, respectively. The improved performance can mainly be attributed to an increased FF and V_{OC}, which originate from improved electron transport and decreased charge recombination.

Finally, the stability of unencapsulated devices was tested (**Fig. 5e**). After 90 days under argon environment at room temperature, P-SnO_2 based PSCs retain 92.2% of their initial PCE, while B-SnO_2 based PSCs still exhibit 97.1%, indicating an increased stability. **Figure 5f** shows the normalized PCE attenuation over 100 h of constant illumination (AM1.5). The device with B-SnO_2 ETL retained 86.5% of its initial performance, while for the PSC with P-SnO_2 this value shrinks to 78.4%. The improved stability may be attributed to the grain size of B-SnO_2 based perovskite films, which is larger than in films grown on P-SnO_2, and may hinder water penetration at grain boundaries. Additionally, at the interface between the ETL and perovskite, P-SnO_2 based devices exhibited more pinholes and defects at the ETL/perovskite interface compared with B-SnO_2 based ones and these defects likely extend with time [38]. This process increases the fraction of grain boundaries and accelerates the rate of deterioration, which is definitively detrimental for the performance.

Conclusions

Our study provides a simple and versatile approach for enhancing the performance and stability of planar perovskite solar cells from the perspective of interfacial engineering. A low temperature processed L-SnO_2/H-SnO_2 bilayer ETL was developed, which induces several beneficial properties, including a better energy level alignment with the CsFAMA perovskite, absence of pinholes in the ETL, improved perovskite film morphology, and enhanced optical absorption. These factors are beneficial for electron extraction and transport, and for reducing undesired charge recombination processes. Mainly the V_{OC} and FF were improved in the PSCs and a maximum PCE of 21.75% was obtained with negligible hysteresis, significantly higher than in the case of pristine SnO_2 based PSCs (max. 18.54%). Moreover, the devices based on the doped bilayer ETL also showed a higher stability both in the dark and under illumination than devices based on single layer ETLs. After 90 days, unencapsulated PSCs using B-SnO_2 retained 97.1% of their initial performance. Additionally, the developed ETLs were fabricated at a temperature as low as 70°C, promoting their application in flexible PSCs and paving the way for the development of tandem devices using for example temperature-sensitive silicon subcells.

AUTHOR INFORMATION

Corresponding Authors

*E-mail: yejiajiu@mail.ustc.edu.cn (Jiajiu Ye), lylliuwhut@whut.edu.cn (Yueli Liu), peter.reiss@cea.fr (Peter Reiss)

Supporting Information

Supporting Information is available from the Wiley Online Library or from the authors.

Acknowledgments

The authors acknowledge the French Research Agency ANR for financial support (Grants SuperSansPlomb ANR-15-CE05-0023-01 and PERSIL ANR-16-CE05-0019-02), and the LABEX Lanef in Grenoble (ANR-10-LABX-51-01) for its support with mutualized instrumentation. The PhD thesis of Yuze Li is funded by UGA IDEX (project IRS C-Super), which is gratefully acknowledged.

Conflict of interest

The authors declare no conflict of interest.

Keywords

perovskite solar cells, electron transport layer, SnO_2, open-circuit voltage

References

[1] Green, M. A.; Ho-Baillie, A.; Snaith, H. J., *Nat. Photonics* **2014,** *8* (7), 506.

[2] Jiang, Q.; Zhao, Y.; Zhang, X.; Yang, X.; Chen, Y.; Chu, Z.; Ye, Q.; Li, X.; Yin, Z.; You, J., *Nat. Photonics* **2019,** *13* (7), 460.

[3] Jeon, N. J.; Na, H.; Jung, E. H.; Yang, T.-Y.; Lee, Y. G.; Kim, G.; Shin, H.-W.; Il Seok, S.; Lee, J.; Seo, J., *Nature Energy* **2018,** *3* (8), 682.

[4] Kim, M.; Kim, G.-H.; Lee, T. K.; Choi, I. W.; Choi, H. W.; Jo, Y.; Yoon, Y. J.; Kim, J. W.; Lee, J.; Huh, D.; Lee, H.; Kwak, S. K.; Kim, J. Y.; Kim, D. S., *Joule* **2019,** *3* (9), 2179.

[5] Lindblad, R.; Bi, D.; Park, B.-w.; Oscarsson, J.; Gorgoi, M.; Siegbahn, H.; Odelius, M.; Johansson, E. M. J.; Rensmo, H., *J. Phys. Chem. Lett.* **2014,** *5* (4), 648.

[6] Ke, W.; Fang, G.; Wang, J.; Qin, P.; Tao, H.; Lei, H.; Liu, Q.; Dai, X.; Zhao, X., *ACS Appl. Mater. Interfaces* **2014,** *6* (18), 15959.

[7] Wang, J. T.-W.; Ball, J. M.; Barea, E. M.; Abate, A.; Alexander-Webber, J. A.; Huang, J.; Saliba, M.; Mora-Sero, I.; Bisquert, J.; Snaith, H. J.; Nicholas, R. J., *Nano Lett.* **2014,** *14* (2), 724.

[8] Tavakoli, M. M.; Yadav, P.; Tavakoli, R.; Kong, J., *Adv. Energy Mater.* **2018,** *8* (23), 1800794.

[9] Zheng, D.; Wang, G.; Huang, W.; Wang, B.; Ke, W.; Logsdon, J. L.; Wang, H.; Wang, Z.; Zhu, W.; Yu, J.; Wasielewski, M. R.; Kanatzidis, M. G.; Marks, T. J.; Facchetti, A., *Adv. Funct. Mater.* **2019,** *29* (16), 1900265.

[11] Méndez, P. F.; Muhammed, S. K. M.; Barea, E. M.; Masi, S.; Mora-Seró, I., *Sol. RRL* **2019,** *3* (9), 1900191.

[12] Dong, Q.; Li, J.; Shi, Y.; Chen, M.; Ono, L. K.; Zhou, K.; Zhang, C.; Qi, Y.; Zhou, Y.; Padture, N. P.; Wang, L., *Adv. Energy Mater.* **2019,** *9* (26), 1900834.

[13] Kogo, A.; Sanehira, Y.; Numata, Y.; Ikegami, M.; Miyasaka, T., *ACS Appl. Mater. Interfaces* **2018,** *10* (3), 2224.

[14] Dong, Q.; Shi, Y.; Wang, K.; Li, Y.; Wang, S.; Zhang, H.; Xing, Y.; Du, Y.; Bai, X.; Ma, T., *J. Phys. Chem. C* **2015,** *119* (19), 10212.

[15] Liu, D.; Wang, Y.; Xu, H.; Zheng, H.; Zhang, T.; Zhang, P.; Wang, F.; Wu, J.; Wang, Z.; Chen, Z.; Li, S., *Sol. RRL* **2019,** *3* (2), 1800292.

[16] Lee, H. B.; Jeon, M.-K.; Kumar, N.; Tyagi, B.; Kang, J.-W., *Adv. Funct. Mater.* **2019,** *29* (32), 1903213.

[17] Yang, G.; Lei, H.; Tao, H.; Zheng, X.; Ma, J.; Liu, Q.; Ke, W.; Chen, Z.; Xiong, L.; Qin, P.; Chen, Z.; Qin, M.; Lu, X.; Yan, Y.; Fang, G., *Small* **2017,** *13* (2), 1601769.

[18] Chen, Y.; Xu, C.; Xiong, J.; Zhang, Z.; Zhang, X.; Yang, J.; Xue, X.; Yang, D.; Zhang, J., *Org. Electron.* **2018,** *58*, 294.

[19] Tang, H.; Cao, Q.; He, Z.; Wang, S.; Han, J.; Li, T.; Gao, B.; Yang, J.; Deng, D.; Li, X., *Sol. RRL* **2020,** *4* (1), 1900415.

[20] Liang, J.; Chen, Z.; Yang, G.; Wang, H.; Ye, F.; Tao, C.; Fang, G., *ACS Appl. Mater. Interfaces* **2019,** *11* (26), 23152.

[21] Liu, Z.; Deng, K.; Hu, J.; Chemie, L. L. J. A., *Angew. Chem. Int. Ed.* **2019,** *131* (33).

[22] Yoo, J. J.; Wieghold, S.; Sponseller, M. C.; Chua, M. R.; Bertram, S. N.; Hartono, N. T. P.; Tresback, J. S.; Hansen, E. C.; Correa-Baena, J.-P.; Bulović, V.; Buonassisi, T.; Shin, S. S.; Bawendi, M. G., *Energy Environ. Sci.* **2019,** *12* (7), 2192.

[23] Zhang, M.; Dai, S.; Chandrabose, S.; Chen, K.; Liu, K.; Qin, M.; Lu, X.; Hodgkiss, J. M.; Zhou, H.; Zhan, X., *J. Am. Chem. Soc.* **2018,** *140* (44), 14938.

[24] Meng, L.; Sun, C.; Wang, R.; Huang, W.; Zhao, Z.; Sun, P.; Huang, T.; Xue, J.; Lee, J.-W.; Zhu, C.; Huang, Y.; Li, Y.; Yang, Y., *J. Am. Chem. Soc.* **2018,** *140* (49), 17255.

[25] Lin, L.; Jones, T. W.; Wang, J. T.-W.; Cook, A.; Pham, N. D.; Duffy, N. W.; Mihaylov, B.; Grigore, M.; Anderson, K. F.; Duck, B. C.; Wang, H.; Pu, J.; Li, J.; Chi, B.; Wilson, G. J., *Small* **2020,** *16* (12), 1901466.

[26] Liu, Z.; Sun, B.; Liu, X.; Han, J.; Ye, H.; Tu, Y.; Chen, C.; Shi, T.; Tang, Z.; Liao, G. J. J. Mater. Chem. A **2018**, 6 (17), 7409.

[27] Yi, H.; Wang, D.; Mahmud, M. A.; Haque, F.; Upama, M. B.; Xu, C.; Duan, L.; Uddin, A., ACS Applied Energy Materials **2018**, 1 (11), 6027-6039.

[28] Wang, H.; Cao, S.; Yang, B.; Li, H.; Wang, M.; Hu, X.; Sun, K.; Zang, Z., *Sol. RRL* **2020,** *4* (1), 1900363.

[29] Xiong, L.; Guo, Y.; Wen, J.; Liu, H.; Yang, G.; Qin, P.; Fang, G., *Adv. Funct. Mater.* **2018,** *28* (35), 1802757.

[30] Singh, M.; Ng, A.; Ren, Z.; Hu, H.; Lin, H.-C.; Chu, C.-W.; Li, G., *Nano Energy* **2019,** *60*, 275.

[29] Song, S.; Kang, G.; Pyeon, L.; Lim, C.; Lee, G.-Y.; Park, T.; Choi, J., *ACS Energy Lett.* **2017,** *2* (12), 2667.

[30] Hanmandlu, C.; Swamy, S.; Singh, A.; Hsin-An, C.; Liu, C.-C.; Lai, C.-S.; Mohapatra, A.; Pao, C.-W.; Chen, P.; Chu, C.-W., *J. Mater. Chem. A* **2020,** *8* (10), 5263.

[31] Wang, Q.; Zu, F.; Caprioglio, P.; Wolff, C. M.; Stolterfoht, M.; Li, M.; Turren-Cruz, S.-H.; Koch, N.; Neher, D.; Abate, A., ACS Energy Letters **2020**, 5 (7), 2343-2348.

[32] Stoumpos, C. C.; Malliakas, C. D.; Kanatzidis, M. G., Inorg. Chem. **2013**, 52 (15), 9019-9038.

[33] Liu, Z.; Deng, K.; Hu, J.; Chemie, L. L. J. A., Angew. Chem. **2019**, 131 (33).

[22] Yi, H.; Wang, D.; Mahmud, M. A.; Haque, F.; Upama, M. B.; Xu, C.; Duan, L.; Uddin, A., ACS Applied Energy Materials **2018**, 1 (11), 6027-6039.

[34] Chen, J.; Bi, Z.; Xu, X.; Yu, H., Electrochim. Acta **2020**, 330, 135197.

[35] Lee, J.-W.; Bae, S.-H.; De Marco, N.; Hsieh, Y.-T.; Dai, Z.; Yang, Y., Materials Today Energy 2018, 7, 149-160.

[36] Zheng, G.; Zhu, C.; Ma, J.; Zhang, X.; Tang, G.; Li, R.; Chen, Y.; Li, L.; Hu, J.; Hong, J.; Chen, Q.; Gao, X.; Zhou, H., Nature Communications 2018, 9 (1), 2793.

[37] Jiang, Q.; Chu, Z.; Wang, P.; Yang, X.; Liu, H.; Wang, Y.; Yin, Z.; Wu, J.; Zhang, X.; You, J., 2017, 29 (46), 1703852.

[38] Sherkar, T. S.; Momblona, C.; Gil-Escrig, L.; Ávila, J.; Sessolo, M.; Bolink, H. J.; Koster, L. J. A., *ACS Energy Letters* **2017,** *2* (5), 1214-1222.